Hindawi Publishing Corporation
EURASIP Journal on Advances in Signal Processing
Volume 2008, Article ID 726854, 14 pages
doi:10.1155/2008/726854

Research Article

Localization Capability of Cooperative Anti-Intruder Radar Systems

Enrico Paolini,[1] Andrea Giorgetti,[1] Marco Chiani,[1] Riccardo Minutolo,[2] and Mauro Montanari[2]

[1] *Wireless Communications Laboratory (WiLAB), Department of Electrical and Computer Engineering (DEIS), University of Bologna, Via Venezia 52, 47023 Cesena, Italy*
[2] *Thales Alenia Space Italia SPA, Land and Joint Systems Division, Via E. Mattei 20, 66013 Chieti, Italy*

Correspondence should be addressed to Marco Chiani, marco.chiani@cnit.it

Received 31 August 2007; Revised 7 January 2008; Accepted 26 March 2008

Recommended by Damien Jourdan

System aspects of an anti-intruder multistatic radar based on impulse radio ultrawideband (UWB) technology are addressed. The investigated system is composed of one transmitting node and at least three receiving nodes, positioned in the surveillance area with the aim of detecting and locating a human intruder (target) that moves inside the area. Such systems, referred to also as UWB radar sensor networks, must satisfy severe power constraints worldwide imposed by, for example, the Federal Communications Commission (FCC) and by the European Commission (EC) power spectral density masks. A single transmitter-receiver pair (bistatic radar) is considered at first. Given the available transmitted power and the capability of the receiving node to resolve the UWB pulses in the time domain, the surveillance area regions where the target is detectable, and those where it is not, are obtained. Moreover, the range estimation error for the transmitter-receiver pair is discussed. By employing this analysis, a multistatic system is then considered, composed of one transmitter and three or four cooperating receivers. For this multistatic system, the impact of the nodes location on area coverage, necessary transmitted power and localization uncertainty is studied, assuming a circular surveillance area. It is highlighted how area coverage and transmitted power, on one side, and localization uncertainty, on the other side, require opposite criteria of nodes placement. Consequently, the need for a system compromising between these factors is shown. Finally, a simple and effective criterion for placing the transmitter and the receivers is drawn.

1. INTRODUCTION

Localization capability is becoming one of the most attractive features of modern wireless network systems. Besides the localization of "friendly" collaborative objects (*tags*), an application that is gaining an increasing attention is the passive geolocation, that is, the possibility of detecting and tracking "enemy" noncollaborative objects (*targets*, typically human beings) within a given area. This application is attractive especially to monitoring critical environments such as power plants, reservoirs or any other critical infrastructure that is vulnerable to attacks. In fact, the protection of these structures requires area monitoring to detect unauthorized human intruders, which is in general difficult and expensive: in this context, a wireless infrastructure composed of cooperative nodes could represent a cheap solution thanks to the advent of high-performance, low-cost signal processing techniques and high-speed networking [1].

Wireless networks for intruder detection and tracking share several common features with those systems known as *multistatic radars* [2]. According to the radar jargon, a radar in which the transmitter and the receiver are colocated is known as a monostatic radar. The expression bistatic radar is used for radar systems which comprise a transmitter and a receiver separated by a distance that is comparable to the target distance [3–5]. In general, bistatic radars are less sensitive than monostatic ones to the near-far target problem, avoid coupling problems between the transmitter and receiver, can detect stealth targets, and are characterized by potentially simple and passive (hence undetectable) receivers. On the other hand, their geometry is more complicated [5], and they require a proper synchronization between the transmitter and the receiver. The expression multistatic radar refers to a radar system with multiple transmitters and/or receivers (e.g., multiple transmitters and one receiver or one transmitter and multiple receivers).

Using multistatic constellations, it is possible to increase the radar sensitivity, to enhance the target classification and recognition, and to decrease the detection losses caused by fading, target scattering directivity and clutter. However, multistatic radars are affected by critical synchronization issues, and require that the transmitters and the receivers share the information (through a network) to cooperatively locate and track the target [6].

A promising wireless technique for anti-intruder cooperative wireless networks is the ultrawideband (UWB) technology. (It will be noticed that UWB signals have been proposed and exploited also for classical monostatic radar systems [7–10].) In USA, a signal is classified as UWB by the Federal Communications Commission (FCC) if it has either a bandwidth larger than 500 MHz or a fractional bandwidth greater than 0.2 [11]; in Europe, it is classified as UWB if its bandwidth is larger than 50 MHz [12]. In anti-intruder cooperative networks, the impulse-radio version of UWB is used, characterized by the transmission of (sub-)nanosecond duration pulses. Usually, the UWB pulses are at a relatively low frequency, between 100 MHz and a few GigaHertz. As a result, the UWB technology can enable to penetrate, through the low-frequency signal spectral components, many common materials (like walls and foliage [13]) while offering an extraordinary resolution and localization precision, due to the large bandwidth. As explained in Section 2, the fundamental block of the target location process in a cooperative wireless network exploiting the impulse radio UWB technology is represented by a ranging process, performed by each receiving node, based on the UWB pulses time of arrival (TOA) estimation [14–18]. The advantages of UWB include, but are not limited to, low-power consumption (battery life), extremely accurate (centimetric) ranging and positioning also in indoor environments, robustness to multipath, low probability to be intercepted (security), large number of devices operating and coexisting in small areas, robustness to narrowband jamming [19].

As from the above discussion, we see that the study of cooperative anti-intruder wireless networks employing impulse radio UWB involves aspects and problems peculiar of different systems, such as multistatic radar systems, wireless sensor networks, and UWB communication systems. Indeed, this is the main reason for, so far, such anti-intruder systems has been presented in the literature under different names like, for example, wireless sensor networks [20], tactical wireless sensor networks [21], multistatic UWB radars [22], and radar sensor networks [23]. Besides area monitoring for human intruder detection, wireless networks based on impulse radio UWB are gaining an increasing interest for a wide spectrum of related applications, like rescue in disaster scenarios [24, 25] (e.g., to quickly localize people trapped in collapsed buildings, or in presence of dense smoke), landmine detection [26], or military applications [21].

In the following section, a cooperative anti-intruder wireless network exploiting the impulse radio UWB will be referred to as an *anti-intruder multistatic UWB radar* or as a *UWB radar sensor network*. At this regard, however, it is worthwhile to pointing out an important different feature between the "traditional" bistatic/multistatic radar (even using UWB signals) and the anti-intruder wireless networks based on impulse radio UWB subject of this work. This difference concerns antennas directivity and the role of the direct radio path between the transmitter and the receiver. In traditional radar systems, the target location process relies on the scattered echo and on the antenna directivity. The direct signal breakthrough between the transmitter and the receiver is harmful to these systems representing a critical issue. On the contrary, the anti-intruder system investigated in the present work employ omnidirectional antennas: as explained in Section 2, the target location process relies on *both* the pulses scattered by the target (echoes) *and* the direct path pulses.

Most of the recent literature on anti-intruder multistatic UWB radars covers either electromagnetic or algorithmic aspects. In the first case, the problem of evaluating the human target radar cross section (RCS) is discussed [27–29]. In the second case, algorithms for target detection and tracking, clutter removal, and extraction of target parameters for classification are proposed [30–33].

Despite this amount of work and the related achievements, there still is a certain knowledge gap with respect to the comprehension of the main system aspects. From this point of view, a critical issue is represented by the necessary compromise between area coverage, required transmitted power, and localization precision as a function of the system geometry and of the nodes position, whose study is particularly of interest for battery-driven nodes and UWB equipments that must satisfy severe power spectral density level restrictions which strongly limit the transmitted power to a few hundreds of microwatts [11, 12]. A second issue, that can be regarded as a subproblem of the previous one, is related to the development of nodes placement criteria, [34], capable of guaranteeing a satisfactory compromise between the above mentioned factors.

This paper investigates an anti-intrusion multistatic UWB radar, with one transmitting (TX) node and multiple receiving (RX) nodes, from such system perspective. The transmitter and the receivers are assumed positioned on the border and/or within the surveillance area with the aim of detecting and locating an intruder that moves inside the area. The scenario and the anti-intruder system are studied in two dimensions with the goal of investigating the impact of the system geometry and nodes position on the coverage percentage, required transmitted power, and localization precision. Numerical results are obtained for a UWB impulse radio system in order to evaluate the location capability offered by this technology in the specific scenario and application considered, which at the authors' knowledge is not present in literature. Based on these numerical results, a simple criterion for nodes location in a circular surveillance area is drawn. In this work, we consider a scenario where only a static clutter is present. A static clutter can be perfectly suppressed, for instance, using the frame-to-frame or the empty-room algorithms described in Section 2: in these conditions, after the clutter removing algorithm, the communication channel becomes equivalent to a additive

white Gaussian noise (AWGN) channel. A nontrivial result obtained in Section 5 is that, even under the hypothesis of a perfect clutter suppression, a system configuration does not exist capable of jointly optimizing the area coverage, the power to be transmitted, and the localization uncertainty. This means that, even under ideal removal clutter conditions, a compromise between these factors must be found.

The paper is organized as follows. A brief system overview is provided in Section 2. Since the basic mechanisms regulating the dependence of area coverage, required transmitted power, and localization uncertainty on the system geometry rely on the single TX-RX pair composing the multistatic system, Section 3 focuses at first on such subsystem (Sections 3.1, 3.2, and 3.3), addressing coverage, power, and ranging uncertainty issues from its perspective. Section 3 then moves to consider the whole system, discussing the required transmitted power and the maximum pulse repetition frequency (PRF) in Section 3.4, and defining the localization uncertainty metric in Section 3.5. This analysis is applied to a multistatic UWB radar system with one TX node and N RX nodes, protecting a circular surveillance area and characterized by a specific nodes location parameterization, in Section 4. For this system, the dependence on the nodes location of area coverage, required transmitted power, and localization uncertainty is investigated in Section 5 for the three and four RX nodes. This analysis leads to the conclusion that the nodes placement criterion must tradeoff the above mentioned factors. A discussion on the obtained results and the main conclusions of our study are given in Section 6.

2. SYSTEM OVERVIEW

The anti-intruder multistatic UWB radar system has the aim of detecting and locating a moving target within a given surveillance area $\mathcal{A}$. It is composed of one TX node and N RX nodes (with $N \geq 3$), where each TX-RX pair can be regarded as a bistatic radar. The transmitter and the multiple receivers could, for example, be placed on the perimeter of the area, as depicted in Figure 1 for circular $\mathcal{A}$.

The target detection and location process comprises a number of subsequent steps, which can be summarized as clutter removal, ranging, detection, imaging, and tracking. The clutter removal and the ranging operations are performed independently by each RX node, while detection, imaging, and tracking are performed by a central node (sometimes referred to as fusion center, not depicted in Figure 1) each RX node is connected with, collecting information by each bistatic radar. It will be noticed that, in the considered system, a hard information is provided by each RX node to the fusion center, namely, indication about target presence or absence and range estimation: the final decision about target presence (alarm) lies within the competence of the fusion center, for example, according to a majority logic. Another possible approach, characterized by a higher complexity both at the RX nodes and at the fusion center, consists in collecting at the fusion center a soft information from each RX node. In this case, the surveillance area is divided into small parts (pixels): for each pixel the generic RX node communicates to the fusion center a soft information outcoming from the correlation between the received signal (as obtained after the clutter removal operation) and the transmitted pulse. This approach is not considered in this paper.

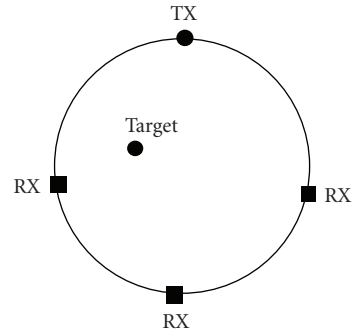

Figure 1: Anti-intruder scenario.

There are several possible algorithms for clutter removal. Simple but effective ones, sketched next, are known as *frame-to-frame* and *empty room* techniques (see, e.g., [35]). The TX node emits sequences of N_s pulses (each pulse having a time duration on the order of the nanosecond): each of these sequences is known as a frame. The system is designed in such a way that the channel response to a single pulse in presence of a moving target does not change appreciably during a frame time, but is different for pulses belonging to subsequent frames. Each emitted pulse of a frame determines the reception by the generic RX node of the direct path pulse followed by pulse replicas due to both the clutter and the target (if present). The estimation, for each of the N_s emitted pulses, of the direct path pulse TOA allows the RX node to perform a coherent average operation of the N_s channel responses, thus reducing by a factor N_s (process gain) the noise power. (It is important to highlight that due to the possibility to accurately estimate the TOA of the first received pulse offered by the impulse radio UWB technology, the RX node does not need any extra synchronization signal for performing the coherent summation of the N_s channel responses, since it extracts the synchronization from the direct signal pulses.)

The frame-to-frame technique consists in performing the above-described coherent average operation over two subsequent frames, and then in taking the sample-by-sample difference between the two obtained signals. Analogously, the empty-room technique consists in performing the above-described operation over one frame, and then in subtracting from the obtained signal the channel response to the single pulse, averaged over N_s pulses, previously obtained in absence of target ("empty room"). In both cases, this operation allows removing the contribution of a static clutter, so that the overall final signal is only due to the thermal noise (with power reduced by a factor N_s) and to the target, if present. In the case of a nonstatic clutter, which is not considered in the present paper, a contribution due to clutter residue will be present too. The decision about the target presence or absence (local detection at the

RX node) is taken using a threshold-based technique. The estimation of the target-scattered pulse (echo) delay with respect to the first path pulse TOA allows the RX node to estimate transmitter-target-receiver range. As pointed out in Section 3.3, an uncertainty in the range estimation is associated with possible TOA estimation errors. Clutter removal techniques more sophisticated than the frame-to-frame one can be adopted, like, for example, the MTD filtering [35] over several subsequent frames.

The hard information received by the central unit from each bistatic radar consists of an indication about the target presence or absence and of a transmitter-target-receiver range estimation. The central unit then performs target detection, eventually aided by the previously obtained tracking information, and target location based on standard trilateration. The target location aims at forming an image of the monitored area with the target position estimated and its trajectory [22]. The position estimation accuracy and false alarm rejection capability can be further improved by means of tracking algorithms [33].

In order to simplify the analysis, it is assumed that only one intruder is present. It is important to explicitly remark, however, that the above described system is capable of detecting and tracking multiple targets. At this regard, two important observations are pointed out next.

First, the possible presence of multiple targets has impact neither on the way to operate of the generic bistatic radar, nor on its complexity. For example, if two moving targets are present within the area, at the end of the frame-to-frame clutter suppression the obtained signal will exhibit two different echoes, each one associated with a specific target: as far as such echoes are resolvable in the delay domain and are both above the detection threshold, the targets are both detected and the corresponding ranges are estimated.

Second, the number of targets to be detected and tracked does not impose a constraint to the minimum required number of RX nodes. More specifically, as far as the generic target satisfies the conditions explained in Section 3 (the target is outside the minimum ellipse and inside the maximum Cassini oval for at least three bistatic radars), it can be detected by the system. Increasing the number of RX node provides benefits in terms of area coverage, and fusion center capability to resolve ambiguous situations where a target is nonresolvable by a bistatic radar. Concerning this issue, it should be observed that the situations where two targets cannot be resolved by a single bistatic radar can be resolved algorithmically at the fusion center (i.e., exploiting the previously obtained tracking information).

On the other hand, with respect to the single target scenario, locating, and tracking multiple targets requires a higher algorithmic complexity (for detection, imaging, and tracking) at the fusion center [23].

Being the perspective target a human being with a velocity of a few meters per second, and being the transmitted signals UWB (with a bandwidth typically larger than 500 MHz), the anti-intruder radar under investigation is not affected by any appreciable Doppler effect. For this reason, when assessing the radar resolution using standard tools like the radar ambiguity function, only the resolution in the delay domain should be considered. The radar ambiguity function was introduced in [36] as a fundamental tool for traditional monostatic narrowband radars. This concept has been more recently extended to narrowband bistatic [37] and multistatic [38] radars, and further to wideband [39] and ultrawideband [7] radars. Highly reminiscent of matched filtering, it provides a synthetic measure of the capability of a given waveform in resolving the target in the delay-Doppler domain, as well of its clutter rejection capability. The radar ambiguity function is effectively used to assess the global resolution and large error properties of the estimates. An alternative approach proposed by several authors is to use the Cramer-Rao bound (CRB) instead of the radar ambiguity function (see, e.g., [40–42]), which represents a local measure of estimation error, affected only by the thermal noise. Indeed, this is the approach followed in this work in order to measure the ranging error estimate, and thus the thickness of the uncertainty annuluses discussed in Section 3.3.

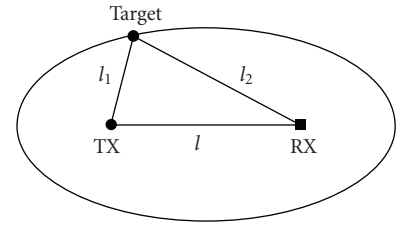

Figure 2: Equi-TOA positions (ellipse) in a bistatic radar.

3. AREA COVERAGE, TRANSMITTED POWER, AND LOCALIZATION UNCERTAINTY

3.1. Equi-TOA and equipower positions for each TX-RX pair

Let us focus on a bistatic radar composed of the generic TX-RX pair, at distance l. We indicate with l_1 and l_2 the distances of the target from the TX node and the RX node, respectively. Assuming line-of-sight (LOS) propagation, if the TX node emits a pulse, this is received at the RX node both through the direct LOS path and after reflection on the target.

The receiver then estimates the TOA of the pulse reflected by the target; based on this, it can estimate the sum distance l_1+l_2. Thus assuming for the moment a perfect TOA estimate, the radar system knows that the target is on the locus of points whose *sum* of the distances from the TX node and the RX node is $l_1 + l_2$, that is, on an ellipse with parameter $l_1 + l_2$ whose foci are the positions of TX and RX, as shown in Figure 2. For each TX-RX pair, we have a family of ellipses, with foci in TX and RX, for all possible values of $l_1 + l_2$ or, equivalently, of the delay of arrival of the target reflected pulse as measured at the receiver (equi-TOA position).

Up to now, we have discussed about the information we can get from the knowledge of the TOA. The peculiar geometry of bistatic radar has also an important impact on the received power for the target reflected pulses. In fact, while in a monostatic radar the received signal power

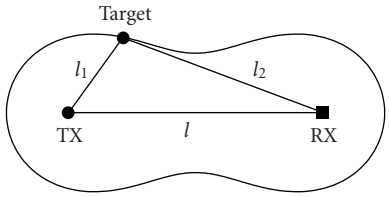

Figure 3: Equi-power positions (Cassini oval) in a bistatic radar.

is proportional to $1/d^4$, where d is the target distance, in a bistatic radar the received power scattered by the target is proportional to $1/(l_1 \cdot l_2)^2$. So, assuming all the other parameters as constant, when a target moves along an equi-TOA ellipse, the delay of the received reflected path does not change, but the received power changes. In particular, on a given equi-TOA ellipse, the lowest received power case is when the target is at the same distance from TX and RX, while more power is received for targets near the foci. From another point of view, we can look at the target positions giving the same received power at the RX node. Geometrically, these positions form the locus of points whose *product* of the distances from the two nodes, $l_1 \cdot l_2$ is constant. This geometric curve is known as *Cassini oval*, with foci in TX and RX. An example of Cassini oval is reported in Figure 3. The Cassini ovals are curves described by points such that the product of their distances from two fixed points a distance $2a$ apart is a constant b^2. The shape of the curve depends on b/a. If $a < b$, then the curve is a single loop with an oval or dog-bone shape. The case $a = b$ produces a lemniscate. If $a > b$, then the curve consists of two loops.

In our scenario, as $l_1 \cdot l_2$ increases (corresponding to a decrease in the received power) the dimension of the ovals increases. By comparing the Cassini ovals tangent to a given ellipse (corresponding to a given TOA), we see that, as previously mentioned, targets near to the foci (TX and RX positions) give rise to a higher-received power. This is illustrated in Figure 4.

3.2. Coverage and target detection for each TX-RX pair

In a bistatic radar with narrowband (NB) pulses, we can evaluate the received power P_r, by using the Friis' formula. For the direct TX-RX path, we have

$$P_{r-\mathrm{NB}}^{\mathrm{direct}} = \frac{P_t G_t G_r \lambda^2}{l^2 (4\pi)^2}, \tag{1}$$

where P_t is the transmitted power, G_t, G_r are the antenna gains at the transmitter and receiver, respectively, and λ is the wavelength.

Let us assume now that the target is characterized by a radar cross section (RCS) σ, defined as [3]

$$\sigma = 4\pi l_2^2 \frac{P_s}{P_i}, \tag{2}$$

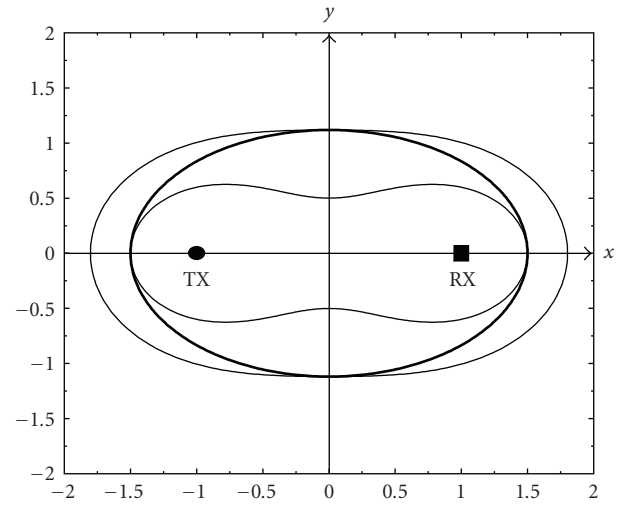

Figure 4: Received power and TOA in bistatic radar: TX and RX are in $(-1, 0)$ and $(1, 0)$, the thick line is an equi-TOA ellipse, the others are Cassini ovals.

where P_i is the incident power density at the target, and P_s is the received power density due to the target scattering. The received power due to the target is then given by [3]

$$P_{r-\mathrm{NB}}^{\mathrm{target}} = \frac{P_t G_t G_r \lambda^2 \sigma}{(4\pi)^3 (l_1 \cdot l_2)^2}. \tag{3}$$

All the previous expressions are for NB signals with all spectral components at (nearly) the same wavelength λ. When using UWB waveforms, this assumption is no longer true since the wavelength can vary considerably within the large band occupied by the transmitted signal. So, in order to evaluate the received power, we should integrate the Friis' formula over all wavelengths of the signal band $[f_L, f_U]$ [43, 44]. From (1) integrated over the UWB band, we obtain the received power of the direct path for the single TX-RX pair as

$$P_{r-\mathrm{UWB}}^{\mathrm{direct}} = \int_{f_L}^{f_L+B} \frac{S_t(f) G_t(f) G_r(f)}{l^2 (4\pi)^2} \left(\frac{c}{f}\right)^2 df, \tag{4}$$

where c is the light speed, $S_t(f)$ is the one-sided transmitted power spectral density, $G_t(f)$, $G_r(f)$ are the frequency-dependent antenna gains, and $B = f_U - f_L$ is the signal bandwidth. Similarly, for the target reflected echo, we have

$$P_{r-\mathrm{UWB}}^{\mathrm{target}} = \int_{f_L}^{f_L+B} \frac{S_t(f) G_t(f) G_r(f) \sigma}{(l_1 \cdot l_2)^2 (4\pi)^3} \left(\frac{c}{f}\right)^2 df. \tag{5}$$

Considering a white spectrum for the transmitted signal and constant antenna gains over $[f_L, f_U]$, (4) becomes

$$P_{r-\mathrm{UWB}}^{\mathrm{direct}} = \frac{S_t G_t G_r c^2}{l^2 (4\pi)^2} \left(\frac{1}{f_L} - \frac{1}{f_L + B}\right), \tag{6}$$

and further considering constant RCS over $[f_L, f_U]$, (5) becomes

$$P_{r-\mathrm{UWB}}^{\mathrm{target}} = \frac{S_t G_t G_r \sigma c^2}{(l_1 \cdot l_2)^2 (4\pi)^3} \left(\frac{1}{f_L} - \frac{1}{f_L + B}\right). \tag{7}$$

These assumptions will be used in the rest of the paper. (The hypothesis of constant antenna gain is realistic for certain UWB antennas [45–47]. The hypotheses of frequency independent transmitted power spectral density and RCS simplify the analysis without affecting the goal of our investigation.)

The extension of the area covered by the generic TX-RX pair present in the system is analyzed next. Let $\mathtt{SNR}_{\text{th}}$ denote the minimum SNR (associated with the target reflected path, and evaluated after the clutter suppression algorithm) required at each RX node to obtain a given detection performance. The value of $\mathtt{SNR}_{\text{th}}$ depends on several factors, such as the specific detector employed and the minimum probability of detection required. Moreover, let PRF denote the pulse repetition frequency, that is the frequency at which the UWB pulses are emitted by the TX node (the maximum pulse repetition frequency will be discussed in Section 3.4). The SNR is related to the one-sided power spectral density N_0 and to the PRF by the relationship

$$\mathtt{SNR} = \frac{N_s P_{r\text{-UWB}}^{\text{target}}}{N_0 \mathtt{PRF}}. \tag{8}$$

In fact, $P_{r\text{-UWB}}^{\text{target}}/\mathtt{PRF}$ represents the received energy per scattered pulse, and the one-sided power spectral density is reduced by the processing gain N_s. Then the condition $\mathtt{SNR} \geq \mathtt{SNR}_{\text{th}}$ leads to

$$P_{r\text{-UWB}}^{\text{target}} \geq P_{\text{th}}, \tag{9}$$

where, by definition, $P_{\text{th}} = \mathtt{SNR}_{\text{th}} N_0 \mathtt{PRF}/N_s$. Assuming a given transmitted power density S_t and letting $P_{r\text{-UWB}}^{\text{target}} = P_{\text{th}}$ in (7), we obtain the maximum value of $l_1 \cdot l_2$ covered by the TX-RX pair, indicated as $(l_1 \cdot l_2)^*$

$$(l_1 \cdot l_2)^* = \sqrt{\frac{S_t G_t G_r \sigma c^2}{P_{\text{th}} (4\pi)^3} \left(\frac{1}{f_L} - \frac{1}{f_L + B} \right)}. \tag{10}$$

We refer to the Cassini oval with parameter $(l_1 \cdot l_2)^*$ as the *maximum Cassini oval* of the TX-RX pair. In a multistatic scenario, a maximum Cassini oval can be defined for each TX-RX pair. So, the first condition a target has to fulfill in order to be detectable by a TX-RX pair is that it must be inside its maximum Cassini oval.

For each TX-RX pair, we also have a condition on the minimum value of $l_1 + l_2$, that is due to the possibility for the RX node to resolve the paths. In fact, the RX node receives the UWB pulses from both the direct path and the target-reflected path. If the delay between the two pulses is too small, the receiver cannot distinguish them. Let us denote with γ the minimum delay in seconds below which the receiver cannot resolve the direct path from the reflected path. So, we must have $(l_1 + l_2) - l \geq \gamma c$, that is,

$$l_1 + l_2 \geq l + \gamma c. \tag{11}$$

Thus a necessary condition for target detection is that the sum of its distances from TX and RX is greater than $l + \gamma c$. The ellipse with parameter $l + \gamma c$ is called the *minimum ellipse*: a target inside the minimum ellipse is invisible to the TX-RX pair.

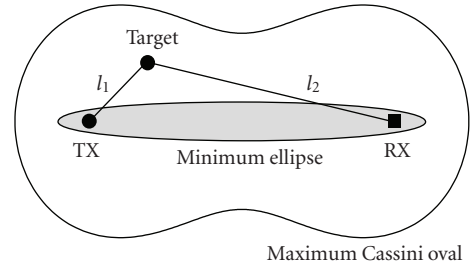

Figure 5: Minimum ellipse and maximum Cassini oval. The area inside the maximum Cassini oval is where the target can be detected. The gray area is a blind zone where targets cannot be detected.

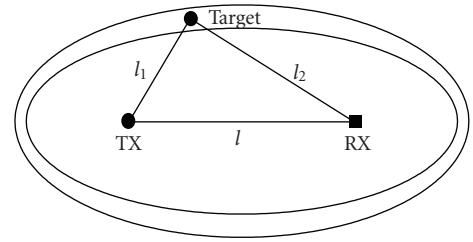

Figure 6: Variable thickness annulus inside which the target is located in presence of imperfect TOA estimation.

By combining the two conditions on the minimum received power and on the minimum delay of arrival, we see that the area where the target can be detected by the generic bistatic radar is inside the maximum Cassini oval, excluding the interior of the minimum ellipse, as sketched in Figure 5.

3.3. Effect of imperfect TOA estimate at each RX node

Let us consider a target detectable for a TX-RX pair. A perfect TOA estimation by the receiver, leading to a perfect estimate of $l_1 + l_2$, allows locating the target on the ellipse with constant $l_1 + l_2$ and foci in TX and RX. However, an imperfect TOA estimation determines an uncertainty on $l_1 + l_2$. In such conditions, the target can be located only inside an *uncertainty annulus* "around" the ellipse with constant $l_1 + l_2$ (see Figure 6).

In general, the annulus depicted in Figure 6 does not have a constant thickness. In fact, the estimation uncertainty depends on the SNR at the receiver, which is not constant for the points of an ellipse with foci in TX and RX as discussed in Section 3.1: the larger the SNR, the smaller the annulus thickness and vice versa. The root mean square error (RMSE) of the distance estimation $\hat{d}$ is lower bounded by the CRB as follows:

$$\sqrt{\mathbb{V}\text{ar}\{\hat{d}\}} \geq \frac{c}{2\sqrt{2}\pi\sqrt{\mathtt{SNR}}\beta}, \tag{12}$$

where $\beta^2 = \int_{-\infty}^{+\infty} f^2 |P(f)|^2 df / \int_{-\infty}^{+\infty} |P(f)|^2 df$, $P(f)$ is the Fourier transform of the transmitted pulse, and where the

SNR is given by (8). In the following, we use (12) to express the thickness of the uncertainty annulus. This approach is effective for sufficiently large values of the SNR. It provides an accurate estimate in the scenario described in Section 5, where the worst-case SNR, namely, $\mathtt{SNR}_{\mathrm{th}}$, is set equal to 10 dB.

3.4. Required-transmitted power and maximum pulse repetition frequency for the multistatic system

Let us consider a Cassini oval with parameter $(l_1 \cdot l_2)^*$. The requirement on the transmitted power spectral density such that a target can be detected by the generic TX-RX pair for any position within the Cassini oval (excluding the interior of the minimum ellipse for the TX-RX pair) follows from (7) and from (9):

$$S_t \geq \frac{P_{\mathrm{th}}\left[(l_1 \cdot l_2)^*\right]^2 (4\pi)^3}{G_t G_r \sigma \left[1/f_L - 1/(f_L + B)\right] c^2}. \tag{13}$$

Hence denoting by $(l_1 \cdot l_2)_{\max}$, the maximum value that $l_1 \cdot l_2$ can assume in the surveillance area $\mathcal{A}$ for the considered TX-RX pair, the RX node is capable to detect a target in any position outside the minimum ellipse if and only if the transmitted power spectral density satisfies (13) with $(l_1 \cdot l_2)^* = (l_1 \cdot l_2)_{\max}$. It is worthwhile observing that $(l_1 \cdot l_2)_{\max}$ depends only on the system geometry and that it is not the same when considering different TX-RX pairs. We denote this value of S_t by $S_{t_{\min}}$, and the corresponding transmitted power by $P_{t_{\min}} = S_{t_{\min}} B$.

For a multistatic system with one TX and N RX nodes, we define

$$(l_1 \cdot l_2)_{\max} = \max_{i=1,\ldots,N} \{(l_1 \cdot l_2)_{\max,i}\}, \tag{14}$$

$$P_{t_{\min}} = \max_{i=1,\ldots,N} \{S_{t_{\min},i}\} \cdot B, \tag{15}$$

where the maximum is taken over all the receiving nodes. If $P_t \geq P_{t_{\min}}$, then each maximum Cassini oval includes the whole surveillance area so that *each* TX-RX pair can detect a target in any area position (excluding the interior of the corresponding minimum ellipse).

Pulses are emitted by the transmitter with a pulse-repetition period T_f, thus $\mathtt{PRF} = 1/T_f$. If a pulse reflected by the target is received before the direct LOS pulse relative to the next pulse period, then the RX node is no longer capable of unambiguously distinguishing between scattered pulses and direct LOS pulses. That leads to the concept of *maximum pulse repetition frequency* ($\mathtt{PRF}_{\max}$).

Let us consider at first a single TX-RX pair. For a given available S_t, a target can be detected for any $l_1 \cdot l_2 \leq (l_1 \cdot l_2)^*$ defined in (10). Let $(l_1 + l_2)^*$ be the maximum $l_1 + l_2$ among all the points for which $l_1 \cdot l_2 \leq (l_1 \cdot l_2)^*$. The maximum propagation time for a reflected pulse from TX to RX is $\tau = (l_1 + l_2)^*/c$. If $P_t = P_{t_{\min}}$, then $(l_1 + l_2)^*$ assumes its maximum value within $\mathcal{A}$, denoted by $(l_1 + l_2)_{\max}$, and $\tau = (l_1 + l_2)_{\max}/c$. As for $(l_1 \cdot l_2)_{\max}$, also $(l_1 + l_2)_{\max}$ depends only on the system geometry and is different for different TX-RX pairs. In any case, the PRF must fulfill $T_f > \tau$, that is, $\mathtt{PRF} < \mathtt{PRF}_{\max}$, where $\mathtt{PRF}_{\max} = 1/\tau$.

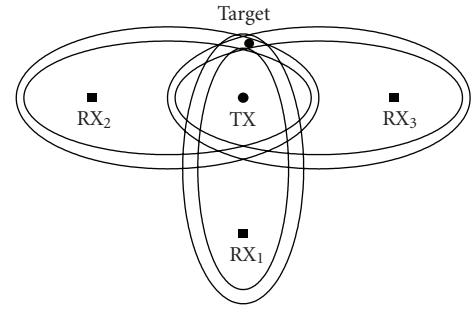

Figure 7: Localization with three receivers and imperfect TOA estimation.

If several RX nodes are present, then

$$(l_1 + l_2)_{\max} = \max_{i=1,\ldots,N} \{(l_1 + l_2)_{\max,i}\}, \tag{16}$$

$$\mathtt{PRF}_{\max} = \frac{c}{(l_1 + l_2)_{\max}}. \tag{17}$$

3.5. Coverage and target localization uncertainty for the multistatic system

It has been pointed out in Section 3.2 that a point of the surveillance area is covered by a single TX-RX pair when it is inside the maximum Cassini oval and outside the minimum ellipse relative to this TX-RX pair. We now say that a point of the surveillance area is covered by the multistatic system, composed of one TX node and $N \geq 3$ RX nodes, when it is covered by at least three TX-RX pairs.

Let us suppose that the TX node and all the RX nodes are characterized by the same threshold $\mathtt{SNR}_{\mathrm{th}}$ and minimum delay γ. A target is localizable when it can be detected by at least three RX nodes located in different positions. With perfect TOA estimation, each RX node locates the target on an ellipse, such that the target position is the intersection point of these ellipses. With imperfect TOA estimation, each RX node can only locate the target within its uncertainty annulus as described in Section 3.3. Hence the system locates the target within the annuluses intersection area, that is, within an *uncertainty area* (see, e.g., in Figure 7 for $N = 3$), which is assumed in this paper as the metric for measuring the overall localization uncertainty. In general, the larger the number of RX nodes covering a certain point, the smaller the uncertainty area in that point. It is worthwhile to noticing that a related study has been carried out in [48, 49] based on the Fisher information, for the localization problem of active nodes through UWB anchors.

4. ANALYSIS OF A MULTISTATIC RADAR

The considerations carried out in Section 3 are here applied to a multistatic UWB radar with one transmitter and N receivers, to study the percentage of area coverage, the required transmitted power and the uncertainty in the target localization process, for different node configurations. We need at least three ellipses to locate the target. With $N = 3$ RX nodes, a target can be localized if and only if it is

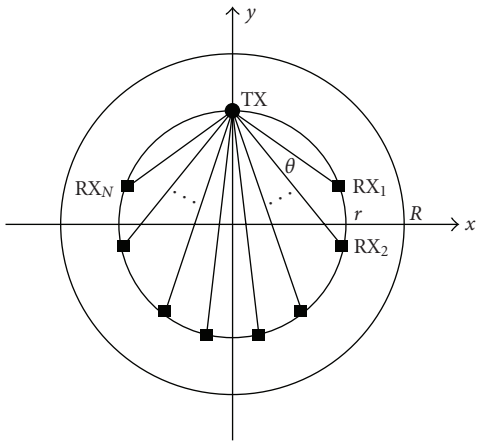

Figure 8: Configuration of N receiving nodes (for even N). The surveillance area $\mathcal{A}$ is the radius-R circle, while the transmitter and the receivers are distributed on a radius-r circle. The angle θ is the same for each pair of contiguous RX nodes and can range between 0 and $\pi/(N-1)$.

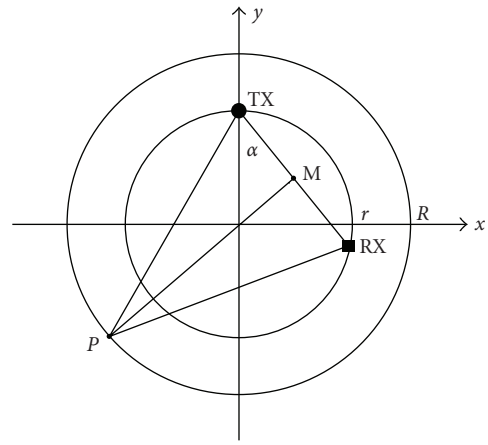

Figure 9: Geometric construction for the computation of $(l_1 \cdot l_2)_{\max}$ and $(l_1 + l_2)_{\max}$ for the depicted TX-RX pair.

inside the three maximum Cassini ovals and outside the three minimum ellipses. Then each maximum Cassini oval must include the whole surveillance area $\mathcal{A}$, that is, we must have $P_t \geq P_{t_{\min}}$ defined in (14). Conversely, with $N \geq 4$, it is sufficient that the target is inside at least three maximum Cassini ovals and outside the corresponding minimum ellipses, so that the constraint $P_t \geq P_{t_{\min}}$ could be relaxed. This fact is addressed in Section 5.2 for the $N = 4$ case.

The analyzed multistatic radar system is depicted in Figure 8 for even N. One TX node and N RX nodes are distributed on a radius-r circle which is concentric with the radius-R circular surveillance area $\mathcal{A}$ ($r \leq R$). The TX node is in the position $(0, r)$, while the RX nodes (indexed from 1 to N as shown in Figure 8) are positioned symmetrically with respect to the y axis with $N/2$ nodes having a positive abscissa and $N/2$ nodes having a negative abscissa. The angle $\text{RX}_i\text{-}\widehat{\text{TX}}\text{-}\text{RX}_{i+1}$ is equal to θ, for all $i = 1, \ldots, N-1$, so that the condition

$$0 \leq \theta \leq \frac{\pi}{N-1} \tag{18}$$

must be fulfilled. For $\theta = 0$, all the RX nodes are in the position $(0, -r)$, while for $\theta = \pi/(N-1)$ RX_1 and RX_N are in the same position as the TX node. For odd N, the analyzed radar system is analogous, with $(N-1)/2$ nodes having a positive abscissa, one node in position $(0, -r)$ and $(N-1)/2$ nodes having a negative abscissa. The same RX nodes indexing is used for odd N.

We show next that for any N the following relationships hold for the parameters discussed in Section 3.4:

$$(l_1 \cdot l_2)_{\max} = R^2 + r^2 + 2Rr \sin\left(\frac{N-1}{2}\theta\right), \tag{19}$$

$$(l_1 + l_2)_{\max} = 2\sqrt{R^2 + r^2 + 2Rr \sin\left(\frac{N-1}{2}\theta\right)}, \tag{20}$$

so that

$$P_{t_{\min}} = \frac{P_{\text{th}}\left[R^2 + r^2 + 2Rr \sin\left(((N-1)/2)\theta\right)\right]^2 (4\pi)^3}{G_t G_r \sigma \left[1/f_L - 1/(f_L + B)\right] c^2} \cdot B, \tag{21}$$

$$\text{PRF}_{\max} = \frac{c}{2\sqrt{R^2 + r^2 + 2Rr \sin\left(((N-1)/2)\theta\right)}}. \tag{22}$$

In fact, let us consider a single TX-RX pair as depicted in Figure 9, where the transmitter has coordinates $x_T = 0$ and $y_T = r$, and where the segment with endpoints M and P is a perpendicular bisector of the segment with endpoints TX and RX. For this TX-RX pair, both $l_1 \cdot l_2$ ($= l_1^2$) and $l_1 + l_2$ ($= 2l_1$) are maximized when the target is in position P. It is readily shown that the point P has coordinates $x_P = -R\cos(\alpha)$ and $y_P = -R\sin(\alpha)$, so that

$$\begin{aligned} l_1 &= \sqrt{(x_P - x_T)^2 + (y_P - y_T)^2} \\ &= \sqrt{R^2 + r^2 + 2Rr \sin(\alpha)}. \end{aligned} \tag{23}$$

Then for the considered TX-RX pair, we have $(l_1 \cdot l_2)_{\max}$ and $(l_1 + l_2)_{\max}$ equal to $R^2 + r^2 + 2Rr\sin(\alpha)$ and $2\sqrt{R^2 + r^2 + 2Rr\sin(\alpha)}$, respectively.

For given r and R, and for α ranging between 0 and $\pi/2$, both $R^2 + r^2 + 2Rr\sin(\alpha)$ and $2\sqrt{R^2 + r^2 + 2Rr\sin(\alpha)}$ are monotonically increasing functions of α. Then among the N RX nodes, those characterized by the largest $(l_1 \cdot l_2)_{\max}$ and $(l_1 + l_2)_{\max}$ are RX_1 and RX_N for both even and odd N. Since for RX_1, we have $\alpha = ((N-1)/2)\theta$ for both even and odd N, we obtain in both cases (19) and (20), which lead to (21) and (22) through (13), (14), and (16).

5. NUMERICAL RESULTS

In this section, numerical results illustrating the system compromise between area coverage, necessary transmitted power, and localization uncertainty are presented for the multistatic radar system described in Section 4, assuming a

Table 1: System parameters.

Parameter	Symbol	Value
Radius	R	50 m
Minimum resolvable delay	γ	1 ns
SNR threshold	$\mathtt{SNR}_{\mathrm{th}}$	10 dB
Lower frequency	f_L	5 GHz
Signal bandwidth	B	500 MHz
Higher frequency	f_U	5.5 GHz
Pulse repetition frequency	PRF	1.5 MHz
Transmitted antenna gain	G_t	0 dB
Received antenna gain	G_r	0 dB
Radar cross-section	σ	1 m^2
Receiver noise figure	F	7 dB
Antenna noise temp.	T_a	290 K
Implementation loss	A_s	2.5 dB

circular surveillance area with radius $R = 50$ m and typical system parameters. As usual for radar sensor networks based on impulse radio UWB, the transmission of short duration pulses with bandwidth $B = 500$ MHz is considered. All the system parameters are shown in Table 1. An additional power attenuation A_s has been considered in (4) and (5). The cases $N = 3$ and $N = 4$ RX nodes are investigated.

The value of the PRF reported in Table 1, $\mathtt{PRF} = 1.5$ MHz, is obtained as the ratio between the the light speed c and the maximum possible value of (20), which is equal to $4R$, corresponding to $r = R$, $\theta = \pi/(N-1)$ and the target in position $(0, -R)$. In all the simulations, this value of the PRF has been used for any target position and nodes location. It guarantees the possibility for each TX-RX pair to unambiguously distinguish between scattered pulses and direct LOS pulses for any target position within the area and any nodes location. The localization uncertainty is evaluated through the method of the uncertainty annulus previously described, where the annulus thickness is computed with the CRB (12).

The localization uncertainty measured as the standard deviation of the estimation error given by the CRB decreases when the SNR increases. It is then possible to reduce the localization uncertainty by acting on the processing gain N_s, as evident from (8). Analogously, the processing gain N_s can be increased to reduce the minimum necessary transmitted power, while keeping the SNR constant from the discussion in Section 2. The numerical results are presented in this section for $N_s = 1$. For $N_s > 1$, the values in dBm of the transmitted power can be obtained by subtracting $10\log_{10}N_s$ from the corresponding values for $N_s = 1$.

This section is organized as follows. The behavior of the area coverage, required transmitted power, and localization uncertainty as functions of the system geometry are presented for a UWB radar sensor network with $N = 3$ RX nodes and $N = 4$ RX nodes in Sections 5.1 and 5.2, respectively. In Section 5.2, it is also emphasized the beneficial effect of using a number of receivers $N > 3$ from the point of view of the transmitted power. Finally, in Section 5.3, the dependence of the localization uncertainty area on the uncertainty annulus thickness, that is, on the range estimation error at the RX nodes, is presented for the case $N = 3$. The curves presented in this subsection are independent of the channel model and on the method adopted for measuring the annuluses thickness. A discussion on the numerical results and the conclusions of the study are presented in Section 6.

5.1. Multistatic radar with three receivers

Let us consider the $N = 3$ case. For $r = 0$, all the nodes are in the same position $(0, 0)$; for $\theta = 0$ the three RX nodes are in the same position $(0, -r)$; for $\theta = \pi/2$ TX, RX_1 and RX_3 are in the same position $(0, r)$. In all these cases, target localization is not possible because three different TX-RX pairs are not available.

In Figure 10, we report the percentage of area coverage, for $P_t = P_{t_{\min}}$ defined in (14) (which means that all the three maximum Cassini ovals cover the whole region $\mathcal{A}$), as a function of r and θ. By definition, one point of the surveillance area is covered, that is a target in that position can be located, if it is inside the three maximum Cassini ovals (this condition is always satisfied for $P_t = P_{t_{\min}}$) and it is outside the three minimum ellipses. For any given θ, the maximum coverage percentage (100%) is tightly approached when $r = 0$, and the minimum coverage percentage is obtained when $r = R$. In fact, for $r = 0$ each of the three minimum ellipses becomes equal to a circumference with center in the origin and radius $c\gamma/2$, whose area is negligible with respect to the surveillance area extension. This maximum must be regarded only as a mathematical limit since target localization is not possible for this configuration. For any given r, the coverage percentage as a function of θ presents two maxima at $\theta = 0$ and $\theta = \pi/2$, and a local minimum. For instance, for $r = R$, the minimum is around $\theta = 15^{\circ}$. Again, the two maxima only represent mathematical limits. In general, the percentage of covered surveillance area is quite high, larger than 80% even for the least favorable pair (r, θ).

The minimum transmitted power $P_{t_{\min}}$, defined in (14) required to obtain the coverage reported in Figure 10, is shown in Figure 11. The minimum transmitted power is an increasing function of both r and θ. From the point of view of the transmitted power, the best configuration is that corresponding to $r = 0$. Analogously to the coverage case, this is only a theoretical optimum, since no localization is possible for this system configuration.

A combined analysis of Figures 10 and 11 leads us to the conclusion that, from the point of view of both the coverage and the transmitted power, the best configurations are characterized by the nodes close to each other, in that r should be kept as small as possible and, for given r, θ should be chosen as small as possible. However, as the receivers get closer, the uncertainty in the target position increases, as shown next.

Let us consider Figure 12, where the intersection region of the uncertainty annuluses is reported as a function of θ, for $P_t = P_{t_{\min}}$ and $r = R$. For each θ, the uncertainty area is evaluated for the worst case target position. The

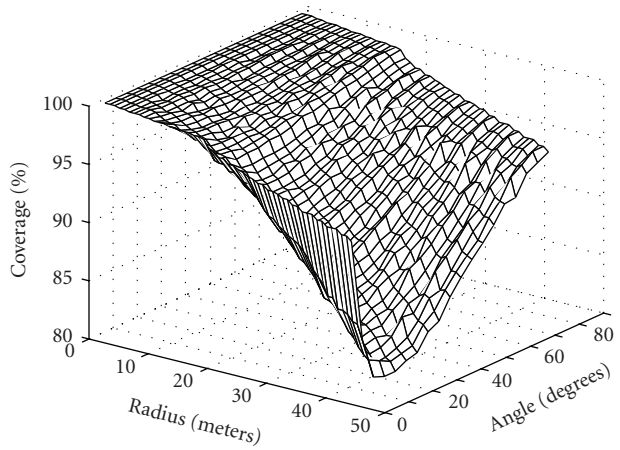

Figure 10: Percentage of covered surveillance area for three receivers as a function of the angle θ and of the radius r ($P_t = P_{t_{\min}}$, $R = 50$ m).

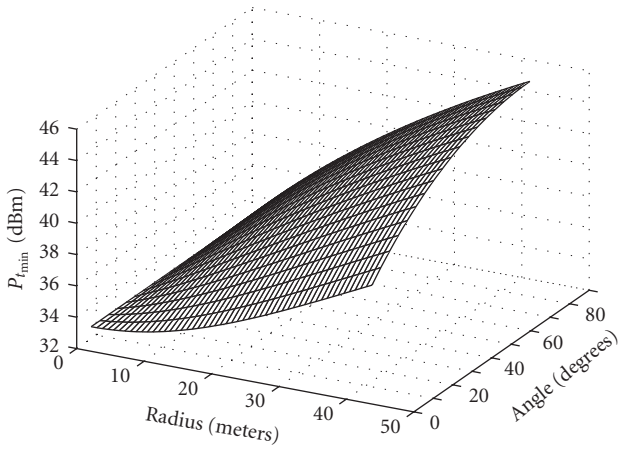

Figure 11: Transmitted power $P_{t_{\min}}$ for three receivers as a function of the angle θ and of the radius r ($R = 50$ m).

uncertainty area increases dramatically for small values of θ. The reason is that, when the RX nodes are very close to each other, the overlapping of the uncertainty annuluses tends to become large. The uncertainty area decreases as θ increases, with a minimum for $\theta \simeq 40^{\circ}$, where the nodes are positioned almost uniformly on the circumference. By further increasing θ, the uncertainty area increases, but slowly. This is the net result of two opposed phenomena: when θ increases, RX_1 and RX_3 get closer, which increases the corresponding annuluses intersection, but they get further from RX_2, which decreases the corresponding annuluses intersection. The worst case uncertainty area is also plotted in Figure 13 as a function of r, for $P_t = P_{t_{\min}}$ and $\theta = \pi/2$. It results a decreasing function of r. Then as opposed to the coverage and transmitted power, from the point of view of the localization precision, the best choice is $r = R$.

The uncertainty area due to the annuluses overlap for the best cases is below cm^2: this confirms the capability of UWB to locate with precision of the order of centimeters.

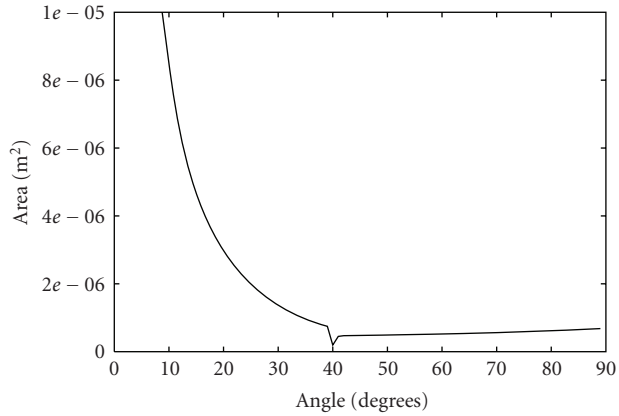

Figure 12: Uncertainty area for three receivers and $r = R = 50$ m, as a function of the angle θ.

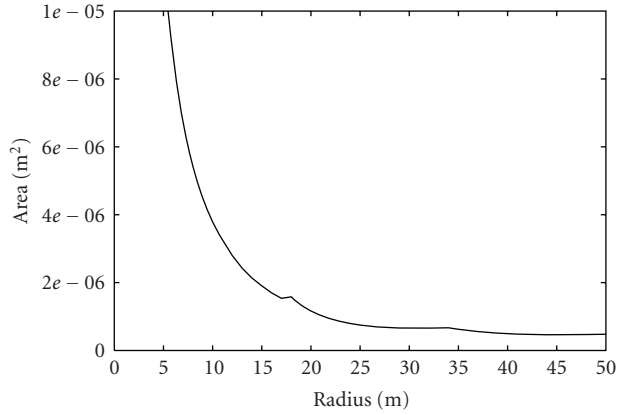

Figure 13: Uncertainty area for three receivers and $\theta = \pi/2$, as a function of the radius r.

5.2. Multistatic radar with four receivers

Numerical results analogous to those presented in Section 4 have been found for $N = 4$ RX nodes. Also in this case, by using a transmission power $P_{t_{\min}}$ (meaning that each maximum Cassini oval covers the whole area), $r = 0$ comes out to be the most convenient choice from the point of view of both the area coverage and the transmitted power. The percentage of area coverage obtained for $P_t = P_{t_{\min}}$ is slightly better than that found in the $N = 3$ case. For instance, for $r = R$ the percentage of area coverage has its minimum at $\theta \simeq 3^{\circ}$, where its value is about 91%. Again, the $r = 0$ configuration must be regarded only as a mathematical limit (no localization is possible), and is the worst configuration from the point of view of the localization uncertainty, which is minimized by $r = R$ and $\theta \simeq 37^{\circ}$.

If the number of RX nodes is equal to three, a necessary condition for locating an intruder within the surveillance area is that each maximum Cassini oval covers the whole area, corresponding to the transmission of a power $P_t = P_{t_{\min}}$ defined in (14). This condition is no longer necessary with a number of RX nodes larger than three. In fact, as recalled in Section 4, it is now sufficient that any point of the

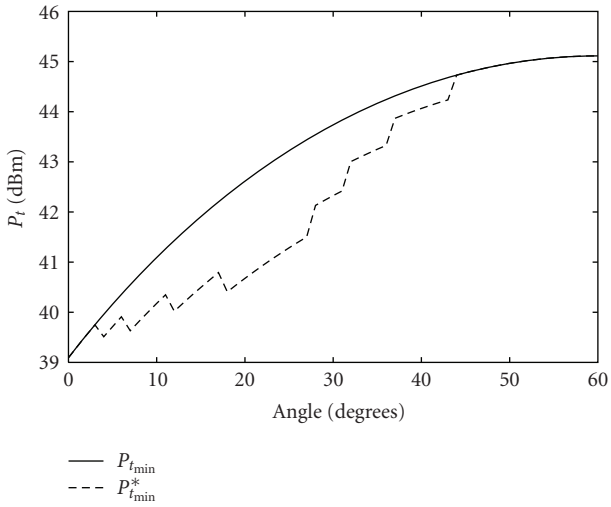

FIGURE 14: Transmitted power $P_{t_{\min}}$ and minimum required transmitted power $P^*_{t_{\min}}$ for having the same area coverage as a function of the angle θ (four receivers, $R = 50$ m).

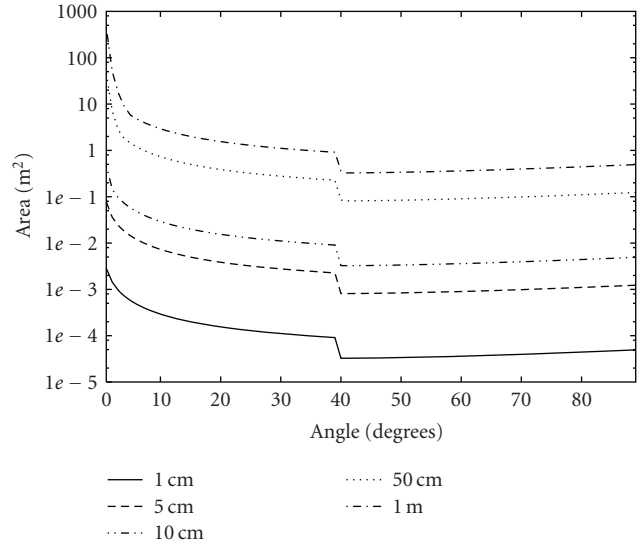

FIGURE 15: Uncertainty area for $N = 3$ receivers and $r = R = 50$ m, as a function of the angle θ and for different annulus thickness values.

surveillance area belongs to at least three maximum Cassini ovals and is outside the corresponding three minimum ellipses. This implies the possibility to obtain the maximum area coverage with a transmitted power $P^*_{t_{\min}}(r, \theta)$ smaller than the power $P_{t_{\min}}$ given in (14) required for covering the whole area with each of the N Cassini ovals. A comparison between $P_{t_{\min}}$ and $P^*_{t_{\min}}$, both expressed as a function of θ, is presented in Figure 14 for $N = 4$ RX nodes, $N_s = 1$ and $r = R$. For some values of θ, the transmitted power can be reduced by one or two dBm.

5.3. Uncertainty annuluses thickness and localization uncertainty

As explained in Section 3.3, an imperfect TOA estimation by an RX node leads to an impossibility, for that node, to locate the target on an ellipse. The RX node can locate the target only inside an uncertainty annulus "around" that ellipse. Being the thickness of this annulus depending on the SNR, and being the SNR not constant along the ellipse, the annulus thickness varies along the ellipse. This phenomenon has been taken into account in the simulation results presented so far, in particular in Figures 12 and 13, where the annulus thickness has been set equal to (12).

An important point is to analyze the degradation of the UWB multistatic radar localization capability as the RX nodes TOA estimation error (i.e., $l_1 + l_2$ estimation error) increases. To this aim, we introduce in this subsection the approximation of constant annulus thickness. Specifically, the uncertainty annulus thickness is considered constant along the ellipse and equal for all the RX nodes. The behavior of the uncertainty area is investigated next as a function of the system geometric parameters, for different thickness values.

In Figures 15 and 16, the worst case uncertainty area is reported, for thickness values 1 cm, 5 cm, 10 cm, 50 cm, and 1 m, for $N = 3$ RX nodes and $P_t = P_{t_{\min}}$. In Figure 15, $r = R$ is assumed and the uncertainty area is plotted as a function of the angle θ, while in Figure 16 $\theta = \pi/2$ is assumed and the uncertainty area is plotted as a function of the radius r. A relevant conclusion which can be deducted by the analysis of these results is that the uncertainty area increases with the annuluses thickness with an approximately linear law.

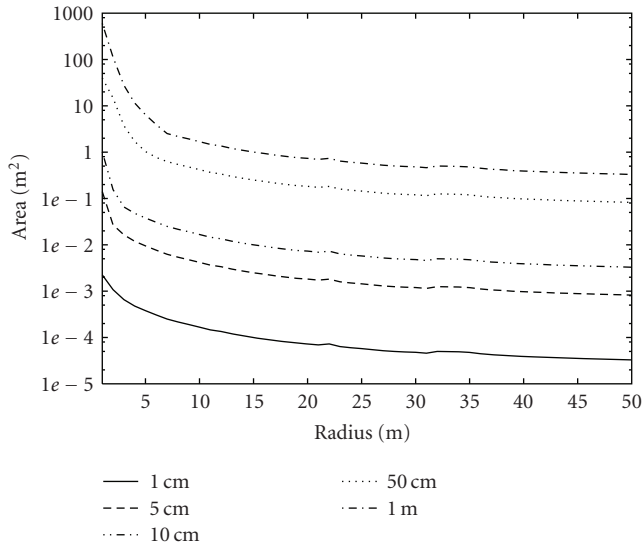

FIGURE 16: Uncertainty area for $N = 3$ receivers and $\theta = \pi/2$, as a function of the radius r and for different annulus thickness values.

An advantage of the results reported in this subsection is to be universal, in that the presented curves, being parametric in the annulus thickness, hold independently of the channel model and of the TOA estimator. For instance, as explained in Section 1, in the presence of a static clutter perfectly removed by one of the clutter suppression algorithms mentioned in Section 2, the communication

channel can be assumed as AWGN. In these conditions, the CRB provides a good estimate of the uncertainty annulus thickness. When these hypotheses cannot be fulfilled or when the SNR is not sufficiently high this is no longer true, being the CRB too optimistic. Tighter inequalities, like the Ziv-Zakai lower bound [50], should be considered for expressing the thickness of the uncertainty annuluses: in these conditions the curves in Figures 15 and 16 remain meaningful because, for a given thickness, they provide the behavior of the uncertainty area independently of the channel model and of which inequality or technique has been chosen for evaluating the annuluses thickness.

6. RESULTS DISCUSSION AND CONCLUSION

The main conclusions of our study are presented and discussed next.

(1) As we have seen in Section 5.2, the power $P_{t_{\min}}$ required for including the whole circular area within each maximum Cassini oval can be larger than the power strictly necessary for obtaining the optimum area coverage. On the other hand, using a power $P_{t_{\min}}$ does not necessarily mean to waste transmission power. It enables having up to N RX nodes available for target localization in any point of the area $\mathcal{A}$. Using $P_t = P_{t_{\min}}$, a TX-RX pair is unavailable in one point only if that point is inside the corresponding minimum ellipse. This is beneficial in terms of both localization precision and system robustness. In fact, the larger the number of available uncertainty annuluses, the smaller their intersection. Moreover, if $L \geq 4$ RX nodes are available for target localization in one point, in that point the target can be still localized even if at most $L - 3$ of such RX nodes are not working.

(2) Assuming $P_t = P_{t_{\min}}$ defined in (14), the configuration corresponding to $r = 0$ is capable of optimizing both the area coverage and the transmitted power. This holds for any N. In fact, if the TX node and the RX nodes are in the same position, then almost complete area coverage is obtained; if this position is the center of the surveillance area ($r = 0$), then the transmitted power is minimized. Then *from the point of view of both area coverage and transmitted power the nodes should be located close to each other around the center of the area*. It is readily shown that the above result is not limited to the case of Figure 8, where r and θ constraints are imposed to the nodes position, but is much more general. Even if the only constraint is that all the nodes must belong to the circular area, for arbitrary number N of RX nodes the power $P_{t_{\min}}$ is minimized when the TX node and all the RX nodes are in the center of the area. In order to show this, it is sufficient to prove that, for a single TX-RX pair, we have

$$\min_{T,R\in\mathcal{A}} \max_{P\in\mathcal{A}} \{l_1 \cdot l_2\} = R^2, \tag{24}$$

where T, R, and P are the TX node, RX node, and target positions, respectively, and where the result is obtained for T and R being the center of the area.

(3) The simulations investigating the radar system localization precision (performed under the r and θ constraints, for $N = 3$ and $N = 4$) have highlighted that the minimum uncertainty is achieved by positioning the nodes as far as possible from the center of the circular area $\mathcal{A}$, that is on the area border. Moreover, they have highlighted that if the nodes are positioned on a circumference concentric with the circular region, a configuration where the nodes are uniformly distributed on this circumference usually guarantees a precision close to the optimum. For $r = R$, in the $N = 3$ case the optimum value of θ is about 40°, where $\theta = 45°$ corresponds to the nodes placed at the vertices of a square. For $r = R$, in the $N = 4$ case the optimum value of θ is about 37°, where $\theta = 36°$ corresponds to the nodes placed at the vertices of a regular pentagon. Then *from the point of view of the target localization precision all the nodes should be located on the border of the area, almost uniformly distributed*.

(4) For an anti-intruder multistatic radar system used to protect a circular area, we then formulate the following simple and provably good criterion for placing the nodes. Given a minimum tolerable localization precision, place the nodes uniformly on a radius-r circle concentric with the area border and choose r as small as possible, compatibly with the precision requirement. If the nodes must be placed on the area border, place them uniformly on it.

ACKNOWLEDGMENTS

This work has been supported in part by the Italian Ministry of Defense, Project IRMA. The authors wish to thank the anonymous reviewers for their valuable comments, and the associate editor Damien Jourdan for handling the review process.

REFERENCES

[1] P. Withington, H. Fluhler, and S. Nag, "Enhancing homeland security with advanced UWB sensors," *IEEE Microwave Magazine*, vol. 4, no. 3, pp. 51–58, 2003.

[2] V. S. Chernyak, *Fundamentals of Multisite Radar Systems*, Gordon and Breach Science, Amsterdam, The Netherlands, 1998.

[3] M. I. Skolnik, *Radar Handbook*, McGraw-Hill Professional, New York, NY, USA, 2nd edition, 1990.

[4] N. J. Willis, *Bistatic Radar*, SciTech, Raleigh, NC, USA, 2nd edition, 2007.

[5] M. C. Jackson, "The geometry of bistatic radar systems," *IEE Proceedings F*, vol. 133, no. 7, pp. 604–612, 1986.

[6] S. Doughty, K. Woodbridge, and C. Baker, "Characterisation of a multistatic radar system," in *Proceedings of the 3rd IEEE European Radar Conference (EuRAD '06)*, pp. 5–8, Manchester, UK, September 2006.

[7] D. E. Iverson, "Coherent processing of ultra-wideband radar signals," *IEE Proceedings—Radar, Sonar and Navigation*, vol. 141, no. 3, pp. 171–179, 1994.

[8] J. D. Taylor, *Introduction to Ultra Wideband Radar Systems*, CRC Press, Boca Raton, Fla, USA, 1995.

[9] J. D. Taylor, *Ultra-Wideband Radar Technology*, CRC Press, Boca Raton, Fla, USA, 2000.

[10] I. I. Immoreev and D. V. Fedotov, "Ultra wideband radar systems: advantages and disadvantages," in *Proceedings of the IEEE Conference on Ultra Wideband Systems and Technologies (UWBST '02)*, pp. 201–205, Baltimore, Md, USA, May 2002.

[11] Federal Communications Commission, "Revision of part 15 of the commission's rules regarding ultra-wideband transmission systems, first report and order (ET Docket 98-153)," April 2002.

[12] Commission of the European Communities, "Commission decision of 21 february 2007 on allowing the use of the radio spectrum for equipment using ultra-wideband technology in a harmonised manner in the community (2007/131/EC)," Official Journal of the European Union, February 2007.

[13] S. Gauthier, E. Hung, and W. Chamma, "Surveillance through concrete walls," Tech. Rep. TM 2003-233, Defence R & D Canada, Ottawa, Canada, 2003.

[14] J.-Y. Lee and R. A. Scholtz, "Ranging in a dense multipath environment using an UWB radio link," *IEEE Journal on Selected Areas in Communications*, vol. 20, no. 9, pp. 1677–1683, 2002.

[15] C. Falsi, D. Dardari, L. Mucchi, and M. Z. Win, "Time of arrival estimation for UWB localizers in realistic environments," *EURASIP Journal on Applied Signal Processing*, vol. 2006, Article ID 32082, 13 pages, 2006.

[16] D. Dardari, C.-C. Chong, and M. Z. Win, "Analysis of threshold-based ToA estimators in UWB channels," in *Proceedings of the 14th European Signal Processing Conference (EUSIPCO '06)*, Florence, Italy, September 2006.

[17] D. B. Jourdan, D. Dardari, and M. Z. Win, "Position error bound and localization accuracy outage in dense cluttered environments," in *Proceedings of the IEEE International Conference on Ultra-Wideband (ICUWB '06)*, pp. 519–524, Waltham, Mass, USA, September 2006.

[18] D. Dardari and M. Z. Win, "Threshold-based time-of-arrival estimators in UWB dense multipath channels," in *Proceedings of the IEEE International Conference on Communications (ICC '06)*, vol. 10, pp. 4723–4728, Istanbul, Turkey, June 2006.

[19] A. Giorgetti, M. Chiani, and M. Z. Win, "The effect of narrowband interference on wideband wireless communication systems," *IEEE Transactions on Communications*, vol. 53, no. 12, pp. 2139–2149, 2005.

[20] B. Parekh and H. Çam, "Minimizing false alarms on intrusion detection for wireless sensor networks in realistic environments," in *Proceedings of the IEEE Military Communications Conference (MILCOM '07)*, Orlando, Fla, USA, October 2007.

[21] L. Li and T. Kunz, "Cooperative node localization for tactical wireless sensor networks," in *Proceedings of the IEEE Military Communications Conference (MILCOM '07)*, Orlando, Fla, USA, October 2007.

[22] T. Sakamoto, "Nonparametric imaging algorithms for UWB pulse radars," Ph.D. dissertation, Kyoto University, Kyoto, Japan, 2005.

[23] H. D. Ly and Q. Liang, "Collaborative multi-target detection in radar sensor networks," in *Proceedings of the IEEE Military Communications Conference (MILCOM '07)*, Orlando, Fla, USA, October 2007.

[24] J. J. Lee and S. Singh, "Using UWB radios as sensors for disaster recovery," in *Proceedings of the IEEE International Conference on Ultra-Wideband (ICUWB '07)*, pp. 311–315, Singapore, September 2007.

[25] A. Nezirovic, A. G. Yarovoy, and L. P. Ligthart, "Experimental verification of human being detection dependency on operational UWB frequency band," in *Proceedings of the IEEE International Conference on Ultra-Wideband (ICUWB '07)*, pp. 305–310, Singapore, September 2007.

[26] M. Sato and K. Yoshida, "Bistatic UWB radar system," in *Proceedings of the IEEE International Conference on Ultra-Wideband (ICUWB '07)*, pp. 62–65, Singapore, September 2007.

[27] L. M. H. Ulander and T. Martin, "Bistatic ultra-wideband SAR for imaging of ground targets under foliage," in *Proceedings of the IEEE International Radar Conference*, pp. 419–423, Arlington, Va, USA, May 2005.

[28] Y. Chevalier, Y. Imbs, B. Beillard, et al., "UWB measurements of canonical targets and RCS determination," in *Ultra-Wideband Short-Pulse Electromagnetics 4*, pp. 329–334, Tel Aviv, Israel, June 1998.

[29] A. E. C. Tan and M. Y. W. Chia, "Measuring human body impulse response using UWB radar," *Electronics Letters*, vol. 41, no. 21, pp. 1193–1194, 2005.

[30] I. Bradaric, G. T. Capraro, D. D. Weiner, and M. C. Wicks, "Multistatic radar systems signal processing," in *Proceedings of the IEEE International Conference on Radar*, pp. 106–113, New York, NY, USA, April 2006.

[31] F. C. B. F. Muller, R. G. Farias, C. L. S. S. Sobrinho, and V. Dmitriev, "Multistatic radar with ultra-wideband pulses: FDTD simulation," in *Proceedings of the SBMO/IEEE International Conference on Microwave and Optoelectronics (IMOC '05)*, pp. 574–577, Brasilia, Brazil, July 2005.

[32] C. Chang and A. Sahai, "Object tracking in a 2D UWB sensor network," in *Proceedings of the 38th Asilomar Conference on Signals, Systems and Computers*, vol. 1, pp. 1252–1256, Pacific Grove, Calif, USA, November 2004.

[33] H. M. M. T. Raza, A. H. Akbar, S. A. Chaudhry, G. Bag, S. W. Yoo, and K. H. Kim, "A yaw rate aware sensor wakeup protocol (YAP) for target prediction and tracking in sensor networks," in *Proceedings of the IEEE Military Communications Conference (MILCOM '07)*, Orlando, Fla, USA, October 2007.

[34] D. B. Jourdan and N. Roy, "Optimal sensor placement for agent localization," in *Proceedings of the IEEE/ION Position Location and Navigation Symposium (PLANS '06)*, pp. 128–139, San Diego, Calif, USA, April 2006.

[35] S. Nag and M. Barnes, "A moving target detection filter for an ultra-wideband radar," in *Proceedings of the IEEE Radar Conference*, pp. 147–153, Huntsville, Ala, USA, May 2003.

[36] P. M. Woodward, *Probability and Information Theory, with Applications to Radar*, Pergamon Press, London, UK, 1953.

[37] T. Tsao, M. Slamani, P. Varshney, D. Weiner, H. Schwarzlander, and S. Borek, "Ambiguity function for a bistatic radar," *IEEE Transactions on Aerospace and Electronic Systems*, vol. 33, no. 3, pp. 1041–1051, 1997.

[38] I. Papoutsis, C. J. Baker, and H. D. Griffiths, "Netted radar and the ambiguity function," in *Proceedings of the IEEE International Radar Conference*, pp. 883–888, Arlington, Va, USA, May 2005.

[39] D. C. Lush and D. A. Hudson, "Ambiguity function analysis of wideband radars," in *Proceedings of the IEEE National Radar Conference*, pp. 16–20, Los Angeles, Calif, USA, March 1991.

[40] Q. Jin, K. M. Wong, and Z.-Q. Luo, "The estimation of time delay and Doppler stretch of wideband signals," *IEEE Transactions on Signal Processing*, vol. 43, no. 4, pp. 904–916, 1995.

[41] A. Dogandzic and A. Nehorai, "Estimating range, velocity, and direction with a radar array," in *Proceedings of the IEEE International Conference on Acoustics, Speech, and Signal Processing (ICASSP '99)*, vol. 5, pp. 2773–2776, Phoenix, Ariz, USA, March 1999.

[42] H. L. V. Trees, K. L. Bell, and Y. Wang, "Bayesian Cramer-Rao bounds for multistatic radar," in *Proceedings of the International Waveform Diversity & Design Conference (IWDCC '06)*, Lihue, Hawaii, USA, January 2006.

[43] R. A. Scholtz, D. M. Pozar, and W. Namgoong, "Ultra-wideband radio," *EURASIP Journal on Applied Signal Processing*, vol. 2005, no. 3, pp. 252–272, 2005.

[44] H. Sheng, P. Orlik, A. M. Haimovich, L. J. Cimini Jr., and J. Zhang, "On the spectral and power requirements for ultra-wideband transmission," in *Proceedings of the IEEE International Conference on Communications (ICC '03)*, vol. 1, pp. 738–742, Anchorage, Alaska, USA, May 2003.

[45] H. G. Schantz, "Introduction to ultra-wideband antennas," in *Proceedings of the IEEE Conference on Ultra Wideband Systems and Technologies*, pp. 1–9, Reston, Va, USA, November 2003.

[46] H. Ghannoum, S. Bories, C. Roblin, and A. Sibille, "Biconical antennas for intrinsic characterization of the UWB channel," in *Proceedings of the IEEE International Workshop on Antenna Technology: Small Antennas and Novel Metamaterials (IWAT '05)*, pp. 101–104, Singapore, March 2005.

[47] A. Sibille, S. Bories, R. D'Errico, and C. Roblin, "UWB antenna performance evaluation from the communication system point of view," in *Proceedings of the 3rd International Symposium on Wireless Communication Systems (ISWCS '06)*, pp. 417–422, Valencia, Spain, September 2006.

[48] Y. Shen and M. Z. Win, "Fundamental limits of wideband localization accuracy via Fisher information," in *Proceedings of the IEEE Wireless Communications and Networking Conference (WCNC '07)*, pp. 3046–3051, Hong Kong, March 2007.

[49] Y. Shen, H. Wymeersch, and M. Z. Win, "Fundamental limits of wideband cooperative localization via Fisher information," in *Proceedings of the IEEE Wireless Communications and Networking Conference (WCNC '07)*, pp. 3951–3955, Hong Kong, March 2007.

[50] D. Dardari, C.-C. Chong, and M. Z. Win, "Improved lower bounds on time-of-arrival estimation error in realistic UWB channels," in *Proceedings of the IEEE International Conference on Ultra-Wideband (ICUWB '06)*, pp. 531–537, Waltham, Mass, USA, September 2006.